XLVI CILAMCE
VITÓRIA - ES - BRAZIL - 2025
XLVI IBERO-LATIN AMERICAN CONGRESS ON COMPUTATIONAL METHODS IN ENGENEERING

The influence of the convergent geometry at the parietal flow behavior in a water tunnel test section

Carlos Henrique Araújo Soldera[1], Augusto Salomão Bornschlegell[1]

[1]*Faculty of Engineering FAEN, University of Grande Dourados UFGD*
Cidade Universitária, Unidade 2, Caixa Postal: 364, CEP: 79.804-970, Dourados - MS, Brazil

Abstract. This study investigates the influence of different convergent geometries on the thermal and hydrodynamic behavior of flow in a water tunnel test section through computational fluid dynamics (CFD) simulations. Three geometric profiles were analyzed: a straight-line profile, a third-order polynomial curve, and a hyperbolic tangent function. The simulations were conducted using OpenFOAM, employing transient formulations of the Navier–Stokes equations and considering temperature-dependent thermophysical properties of water. Results showed negligible differences in temperature distribution across the geometries; however, significant variations were observed in pressure and velocity fields. The hyperbolic tangent profile demonstrated superior performance, promoting uniform flow, reduced pressure gradients, and faster boundary layer development. These findings highlight the importance of smooth, continuous convergent shapes in achieving flow stability and uniformity in experimental test sections.

Keywords: Water tunnel, CFD, Convergent geometry.

1 Introduction

Water tunnels are research tools which have been used extensively for the study of fluid mechanics, where experiments can be carried out under different and controlled conditions. Among them, it is worth mentioning the flow turbulence and velocity profile. In addition, in studies focused on parietal flow, it is important to ensure uniformity in the regions near the walls [1].

Among the different sections of a water tunnel, the convergent plays a key role in establishing uniform flow conditions. It gradually narrows the passage through which the fluid travels from the settling chamber to the test section. As the flow moves through this region, the smooth curvature of the convergent helps to accelerate the fluid, reduce turbulence, and shape a more uniform velocity profile.[2][3].

It is important that the convergent of a water tunnel be designed with smooth and continuous curves, in order to ensure a flow without recirculation zones and without boundary layer separation. Such curves are usually constructed using third- or fifth-order polynomial functions that preserve these characteristics at the inlet and outlet of the convergent, ensuring a gradual flow transition from the settling chamber to the test section, as recommended by Bell e Metha [4] and applied by Nuñez [5].

The aim of this work is to numerically assess the flow behavior near the walls of a water tunnel test section, considering the influence of the convergent geometry.

2 Numerical model

2.1 Geometry and boundary conditions

The convergent section analyzed in this work has a three-dimensional geometry with axial symmetry and a square cross-section, reducing the flow area from the settling chamber to the test section with a contraction ratio of 9:1. Taking advantage of the symmetry, only one quarter of the full geometry was modeled in order to simplify the numerical domain and reduce computational simulation costs, this geometry can be seen in figure 1.

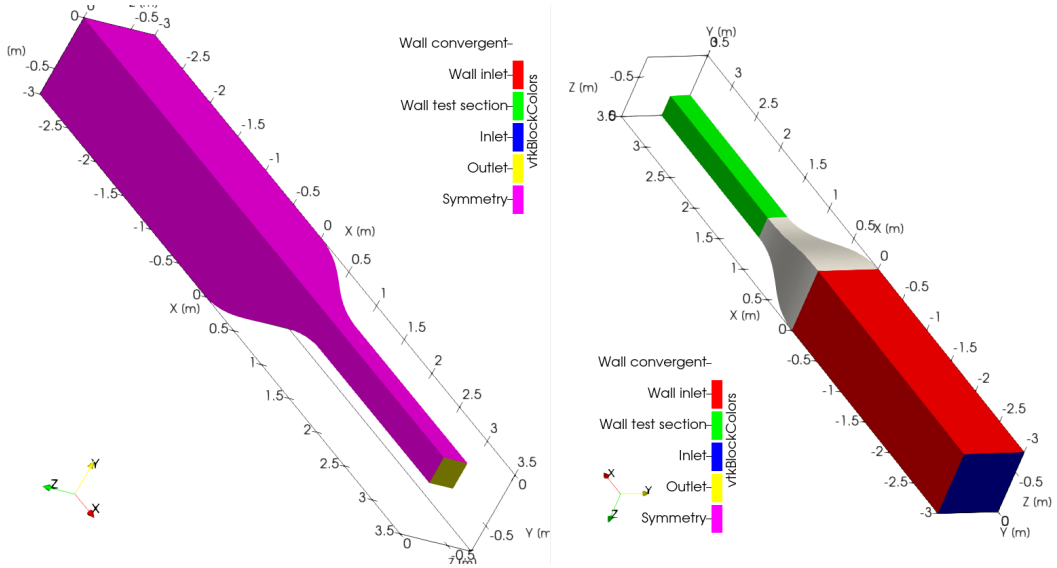


Figure 1. one quarter of the tunnel geometry

Considering the objective of this study, three curvature profiles will be evaluated: one defined by a third-order polynomial function, as proposed by Bell e Metha [4]; another based on a hyperbolic tangent function; and a straight-line profile [6]. These three profiles can be observed in Figure 2.

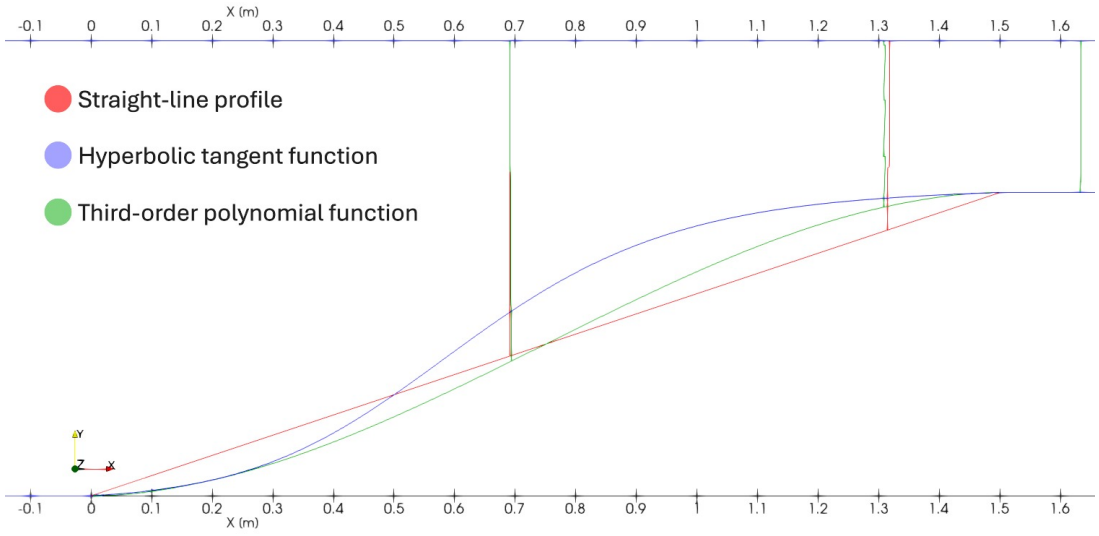


Figure 2. curvature profiles

2.2 Mesh and mesh sensibility

To represent the domain of the convergent section, a three-dimensional mesh was generated using the blockMesh tool available in OpenFOAM. The mesh was composed of structured hexahedral cells. In order to ensure that the simulation results were not influenced by mesh resolution, three mesh levels were tested: coarse, intermediate, and fine (M3, M2 and M1 respectively). Table 1 presents the total number of cells in each case, along with the values of skewness (a measure of cell distortion), mesh quality index (r), shear stress, measured at the entrance of the test section (x=1.5m), and the Grid Convergence Index (GCI), which were used as reference metrics for the comparative analysis.

The mesh refinement was created following the approach proposed by Celik [7]. The ratio between the cell sizes for meshes M1, M2, and M3 was set to $r = 1.3$. From Table 1 , it can be observed that the improvement in mesh quality is more significant from M3 to M2, whereas the difference between M2 and M1 is not as substantial.

Figure 3, obtained from OpenFOAM using ParaView, illustrates the difference in mesh quality between M1,

Table 1. Comparison between different meshes used in the simulation.

Mesh	Cells	Skewness	r	Shear Stress at x=1.5m (Pa)	GCI
M1	4 480 000	0.08	1.30	14.5521	0.01%
M2	2 045 505	0.1	1.30	14.2169	18.8%
M3	922 465	0.13	n.a.	0.03509	n.a.

M2, and M3.

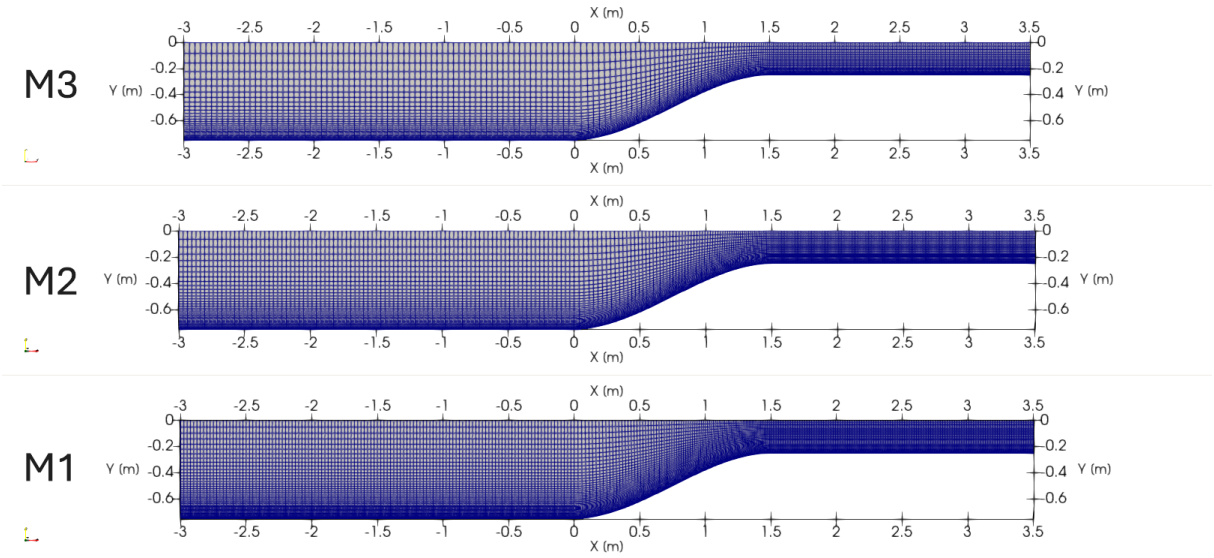


Figure 3. Mesh sensibility Analysis

Since, in the present work, the objective is related to parietal phenomena, the refinement level M1 was selected to run the simulations. No relevant tridimensional phenomena was observed in the tridimensional results. Thus, to further reduce computational effort, a 2D version of the M1 mesh was used.

2.3 Thermophysical Properties

The thermophysical properties of water used in this study were defined as seventh-order temperature-dependent polynomial functions. The specific heat at constant pressure, $c_p(T)$, was defined using the following function:

$$c_p(T) = a_0 + a_1 T + a_2 T^2 + a_3 T^3 + \ldots + a_7 T^7 \tag{1}$$

In this case, the coefficients used were:

$$c_p(T) = 9850.69 - 48.6714\,T + 0.13736\,T^2 - 1.27063 \times 10^{-4}\,T^3 \tag{2}$$

The coefficients associated with higher-order terms (a_4 to a_7) were considered zero due to their insignificantly low values, which would not affect the overall accuracy of the property calculation within the studied temperature range. Standard entropy (S_f) and formation enthalpy (H_f) were also set to zero, since the study does not involve phase changes or chemical reactions.

Similarly, the temperature-dependent density was expressed as:

$$\rho(T) = 746.025 + 1.93017\,T - 3.65471 \times 10^{-3}\,T^2 \tag{3}$$

For the dynamic viscosity $\mu(T)$ and thermal conductivity $\kappa(T)$, the following polynomials were used:

$$\mu(T) = 0.116947 - 0.00100532\,T + 2.90283 \times 10^{-6}\,T^2 - 2.80572 \times 10^{-9}\,T^3 \tag{4}$$

$$\kappa(T) = -0.710696 + 0.0071857\,T - 9.29827 \times 10^{-6}\,T^2 \tag{5}$$

2.4 Numerical schemes

The flow inside the water tunnel was simulated by using the fluid solver available in OpenFOAM version 12, configured to solve the Navier–Stokes equations in three spatial directions (x-axis, y-axis, and z-axis). These equations govern the conservation of momentum over time and were applied in a transient (time-dependent) formulation. Since the model was reduced to a bidimensional domain, the equation in the z-axis was diregarded by the instruction empty at the boundary conditions.

The fundamental equations used in the simulation are the momentum equation 6, the energy equation 7, and the continuity equation 8, which ensure the physical consistency of the model:

$$\frac{\partial \rho u_i}{\partial t} + \frac{\partial}{\partial x_j}(\rho u_j u_i) = -\frac{\partial \rho r g h}{\partial x_i} - \frac{\partial \rho g x_j}{\partial x_i} + \frac{\partial \tau_{ij}}{\partial x_j} \tag{6}$$

$$\frac{\partial \rho h}{\partial t} + \frac{\partial}{\partial x_j}(\rho u_j h) + \frac{\partial \rho k}{\partial t} + \frac{\partial}{\partial x_j}(\rho u_j k) = -\frac{\partial q_i}{\partial x_i} + \rho r + \frac{\partial p}{\partial t} - \rho g_j u_j + \frac{\partial \tau_{ij} u_i}{\partial x_j} \tag{7}$$

$$\frac{\partial \rho}{\partial t} + \frac{\partial \rho u_i}{\partial x_j} = 0 \tag{8}$$

A second-order implicit time discretization scheme "backward" was adopted to ensure both numerical stability and temporal accuracy. The maximum Courant number was set to $Co_{max} = 1$, which helps to keep the time step within stable limits.

To account for the variation of the thermophysical properties due to temperature variatios, they were modeled in function of the temperature. The advective terms were discretized using the "linearUpwind" scheme with second-order accuracy. The pressure–velocity coupling was resolved with the "PIMPLE" algorithm, a hybrid method combining "PISO" and "SIMPLE" strategies, allowing for efficient convergence in transient simulations [8].

Regarding the boundary conditions, at the inlet, it is imposed 0.37 m/s which leads to the project volumetric flow of 3000 m/h. It is also considered the turbulence intensity of 1 % and constant pressure gradient. At the symmetry plane, the symmetry boundary condition is imposed. At the outlet, the pressure of 0.1 MPa is imposed to simulate the atmospheric pressure. Along the walls, the no slip boundary condition and constant pressure gradient are applied.

3 Results and discussion

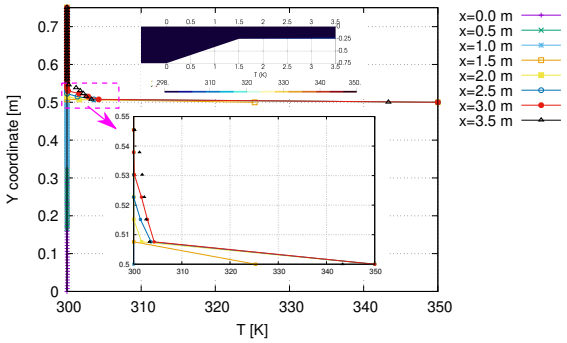
From the numerical simulations carried out, temperature, pressure, and velocity fields were obtained for the three convergent geometries evaluated: straight-line profile, third-order polynomial profile, and hyperbolic tangent profile. This section discusses the influence of each geometry on the stability and uniformity of the flow in the test section.

3.1 Temperature Distribution

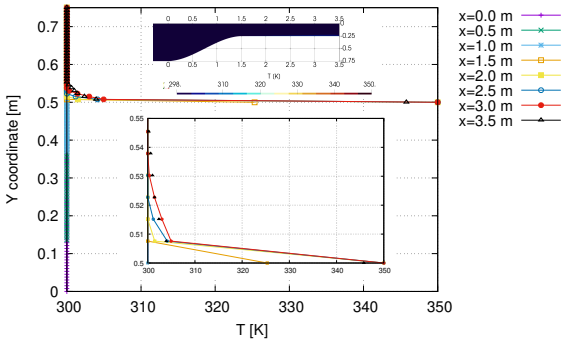
The temperature profiles were analyzed as a function of the vertical coordinate Y, at various axial positions X. As shown in Figure 4, all three geometries — straight, polynomial, and hyperbolic tangent — produced remarkably similar results. This observation suggests that, under the boundary conditions and simulation parameters adopted in this work, the curvature of the convergent section did not significantly influence the thermal distribution in the domain. Therefore, from a thermal standpoint, all three geometries proved equally effective in promoting a stable and homogeneous temperature profile.

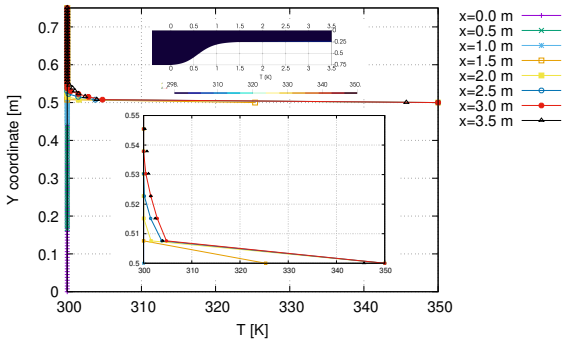
Figure 4. Temperature Graphics

(a) Straight-line profile.



(b) Third-order polynomial function.





(c) Hyperbolic tangent function.

3.2 Pressure Distribution

The pressure fields exhibited more distinct behavior among the geometries, as seen in Figure 5. The straight convergent profile presented the largest pressure gradients and pressure variations, Thus, it presented the highest head losses. The third-order polynomial profile showed improved behavior, with more gradual transitions in pressure along the domain.

However, the hyperbolic tangent profile yielded the most uniform pressure distribution, with smooth gradients and no abrupt variations. These results reinforce the importance of using smoothly curved geometries to reduce pressure gradients and promote steady flow development.

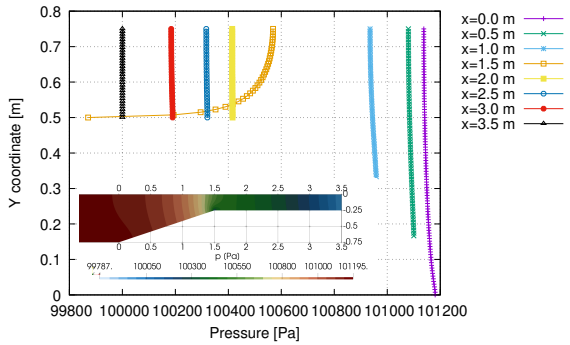
3.3 Velocity Distribution

The analysis of the streamwise velocity component U_x, illustrated in Figure 6, revealed significant differences between the geometries. The straight profile led to more dispersed velocity curves across different axial positions, indicating a slower development of the boundary layer and less uniform flow.

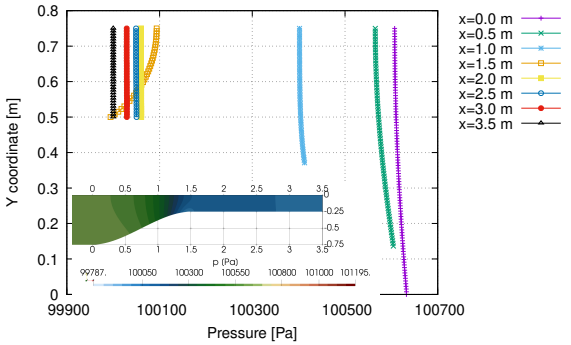
In contrast, the polynomial profile produced a more balanced transition, improving vertical uniformity in intermediate regions. The hyperbolic tangent profile stood out as the most efficient, showing nearly overlapping curves even in the early stages of the test section. This indicates that the flow becomes fully developed more rapidly, confirming that smoothly curved convergent geometries facilitate the establishment of a stable and homogeneous velocity profile throughout the domain.

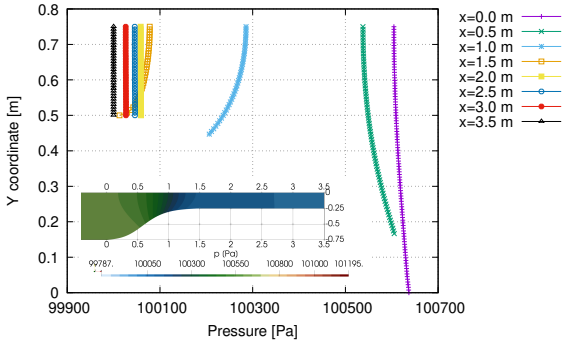
Figure 5. Presure Graphics

(a) Straight-line profile.



(b) Third-order polynomial function.

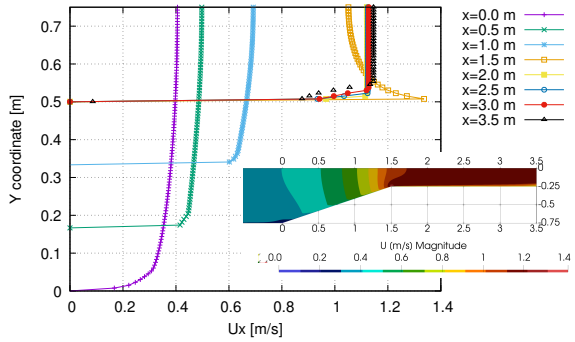




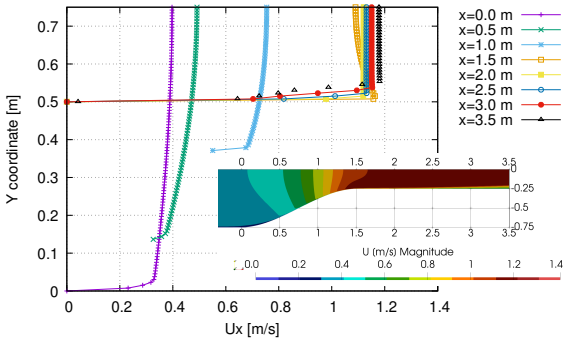
(c) Hyperbolic tangent function.

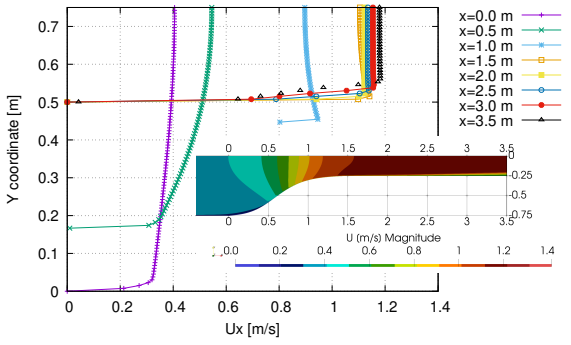
Figure 6. Velocity Graphics

(a) Straight-line profile.



(b) Third-order polynomial function.





(c) Hyperbolic tangent function.

4 Conclusions

This study numerically evaluated the influence of different convergent geometries on the thermal and hydrodynamic behavior of the flow in a water tunnel test section. Three configurations were analyzed: a straight profile, a third-order polynomial curve, and a hyperbolic tangent profile.

The results showed that the temperature distribution was not significantly affected by the chosen geometry, with all profiles exhibiting similar thermal behavior under the defined conditions. In contrast, the pressure and velocity fields demonstrated notable differences. The straight profile produced greater variations and non-uniformity in the flow, while the polynomial profile offered a smoother development. The hyperbolic tangent geometry delivered the best performance, with more uniform and stable pressure and velocity distributions.

Based on the results presented, it can be concluded that designing convergent sections with smooth and continuous curves is essential to promote efficient boundary layer development and also to prevent recirculation zones or flow disturbances. This geometric choice contributes to achieving more stable and well-conditioned flow within the water tunnel test section.

Acknowledgements. The authors acknowledge the National Laboratory for Scientific Computing (LNCC/MCTI, Brazil), through the ambassador program (UFGD), subproject MNSE for providing HPC resources of the SDumont supercomputer, which have contributed to the research results reported within this paper. URL: http://sdumont.lncc.br.

Authorship statement. The authors hereby confirm that they are the sole liable persons responsible for the authorship of this work, and that all material that has been herein included as part of the present paper is either the property (and authorship) of the authors, or has the permission of the owners to be included here.

References

[1] H. Schlichting and K. Gersten. *Boundary-Layer Theory*. Springer, Berlin, 9th edition, 2016.
[2] A. Abdelhamed, Y.-S. Yassen, and M. ElSakka. Design optimization of three dimensional geometry of wind tunnel contraction. *Ain Shams Engineering Journal*, vol. 6, n. 1, pp. 281–288, 2015.
[3] W. Schinestzki, L. Luz, da A. Silva, and J. Ignacio Gonçalves Zart. Projeto conceitual de tunel de vento aerodinâmico de sucção. In *Congresso Aeroespacial Brasileiro*, 2019.
[4] J. Bell and R. Mehta. Contraction design for small low-speed wind tunnels. Technical report, NASA, 1988.
[5] G. Nuñez. Projeto de um tunel de vento de baixas velocidades para o ensino de engenharia do vento - design of a low-speed wind tunnel for wind engineering teaching. *Revista de Ensino de Engenharia*, vol. 40, pp. 394, 2021.
[6] R. J. M. A. Josias Paulucio. Tiburcio. Túnel de vento: projeto, construção e instrumentação, 2021.
[7] I. Celik, U. Ghia, P. Roache, C. Freitas, H. Coloman, and P. Raad. Procedure of estimation and reporting of uncertainty due to discretization in cfd applications. *J. Fluids Eng.*, vol. 130, pp. 078001, 2008.
[8] C. Greenshields and H. Weller. *Notes on Computational Fluid Dynamics: General Principles*. CFD Direct Ltd, Reading, UK, 2022.